

High-Resolution Thermal Simulation Framework for Extrusion-based Additive Manufacturing of Complex Geometries

Dhruv Gamdha^a, Kumar Saurabh^a, Baskar Ganapathysubramanian^{a,*}, Adarsh Krishnamurthy^{a,*}

^aIowa State University, Ames, Iowa, USA

Abstract

Accurate simulation of the printing process is essential for improving print quality, reducing waste, and optimizing the printing parameters of extrusion-based additive manufacturing. Traditional additive manufacturing simulations are very compute-intensive and are not scalable to simulate even moderately sized geometries. In this paper, we propose a general framework for creating a digital twin of the dynamic printing process by performing physics simulations with the intermediate print geometries. Our framework takes a general extrusion-based additive manufacturing G-code, generates an analysis-suitable voxelized geometry representation from the print schedule, and performs physics-based (transient thermal) simulations of the printing process. Our approach leverages adaptive octree meshes for both geometry representation as well as for fast simulations to address real-time predictions. We demonstrate the effectiveness of our method by simulating the printing of complex geometries at high voxel resolutions with both sparse and dense infills. Our results show that this approach scales to high voxel resolutions and can predict the transient heat distribution as the print progresses. Because the simulation runs faster than real print time, the same engine could, in principle, feed thermal predictions back to the machine controller (e.g., to adjust fan speed or extrusion rate). The present study establishes the computational foundations for a real-time *digital twin*, which can be used for closed control loop control in the future.

Keywords: Fused Deposition Modeling, Thermal Simulations, Voxel-by-voxel Printing, Adaptive Octree

1. Introduction

Fused deposition modeling (FDM) is an additive manufacturing process that builds 3D objects layer-by-layer by melting and extruding thermoplastic filaments through a heated nozzle. The nozzle moves along a predetermined path, depositing the molten material in precise locations to create the desired shape. Once deposited, the material then solidifies to create the final part. FDM is a popular and widely used technology due to its low cost, versatility, and ease of use. It can produce parts with good mechanical properties and accuracy. Such 3D printing approaches have revolutionized the manufacturing industry by enabling the production of complex geometries with high precision and customization. However, FDM faces a few challenges in achieving the desired print quality and reducing material waste, especially for complex geometries with sparse infills. One challenge is the need for support structures for overhanging features or complex geometries, which can increase material waste and post-processing time. Another is the possibility of warping and distortion due to thermal stresses during printing, which can affect the final dimensional accuracy of the part.

Accurate simulation of the 3D printing process can help address these challenges by predicting the thermal and mechanical stress distribution as the build progresses, which can inform print quality and material usage. Fast and accurate simulations can help rapidly explore the print process and design non-trivial approaches that minimize material usage while ensuring that thermal stresses are kept to acceptable levels. The ability of real-time simulations also opens up the possibility of creating digital twins of the 3D print process. These digital twins can assimilate measurements from the physical build and accurately predict the intermediate and final shapes. Additionally, once the computed

*Corresponding Authors

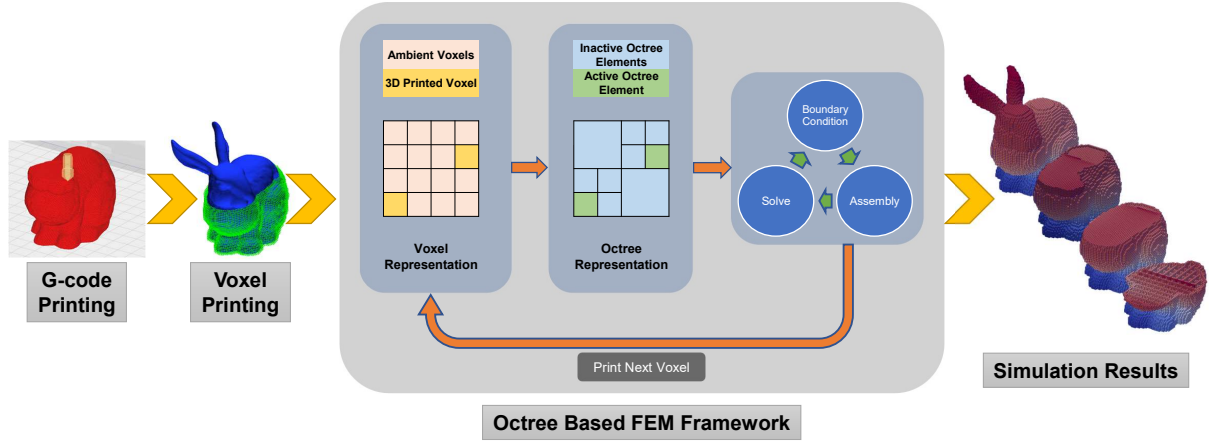


Figure 1: Illustration of the proposed voxel-based, octree-enabled FEM framework for real-time 3D-printing simulations. Starting from a standard G-code model (left), the part is converted into a voxel representation where each newly deposited voxel (green) expands the active region. An octree mesh (center) then refines or coarsens elements based on print progression, enabling efficient assembly and solution of the evolving thermal problem. Finally, the simulation iterates this deposition-and-solve process until the full 3D object (right) is printed.

temperature field can be returned in near-real-time, the same framework could drive model-predictive adjustments to fan speed, extrusion rate, or chamber temperature, thereby closing the control loop.

Simulating the 3D printing process is challenging for several reasons. These include computational challenges associated with (a) efficiently representing complex print geometries, (b) the multiscale nature of the process (small time scales of the nozzle-print interaction vs. long simulation time horizon of the entire print), (c) the coupled multi-physics phenomena (thermal, phase-change, mechanical), and (d) the time- and location-dependent material properties of the print, as well as the complexities of the print schedule (intricate infill patterns, variable resolution, variable material feeds). A final challenge is to simulate the time-dependent printing process in print-time, i.e., faster than the physical print process, to enable control and fast design exploration.

Simulating 3D printing remains a very active research area, with several approaches that resolve some (but not all) of these challenges. Recently, voxel-based methods have emerged as a promising approach for simulating 3D printing, with the possibility of resolving all the challenges listed above. In voxel-based methods, the geometry is represented as a collection of voxels (i.e., volumetric pixels) that capture the printing order (and infill patterns) and material properties. Voxel-based simulations have the advantage of being computationally efficient and flexible in representing complex geometries with arbitrary infill patterns, and the structured representation offers the possibility of fast simulations. In this paper, we propose a novel framework for voxel-by-voxel 3D printing simulation that leverages adaptive octree meshes to efficiently represent the geometry and ensure highly optimized physics simulations. Our framework consists of three distinct stages, as shown in Figure 1:

- Converting GCode into an intermediate voxel representation. We first convert the GCode into a voxel-by-voxel (abbreviated as *VbV*) print schedule. This intermediate representation is flexible enough to account for sparse and dense infill patterns.
- Converting the intermediate voxel representation into an analysis-suitable octree representation, with graceful adaptive coarsening and refinement as the print schedule progresses.
- A scalable FEM simulator based on adaptive octree meshes that predicts transient thermal fields during the print process.

Although the present paper demonstrates only the forward (simulation) path, the achieved speed-ups mean that the solver output is already fast enough to be consumed by an external controller in a future closed-loop implementation. We first compare our framework with experimental data for single filament rectangular geometry and, finally, demonstrate the effectiveness of our framework using several complex geometries at high voxel resolution and under different infill

conditions. To the best of our knowledge, our approach is the first to produce high-fidelity, real-print-time simulations of the 3D printing process for complex geometries by leveraging parallel adaptive octree meshes for FEM-based time-dependent 3D simulations.

The remainder of this paper is structured as follows: in [Section 2](#), we review the existing literature on 3D printing simulations, voxel-based representations, and physics-based modeling. [Section 3](#) describes the methodology of our approach, including the details of each of the three stages. [Section 4](#) presents the results of our simulations and compares them to existing methods or benchmarks, if available. Finally, we discuss the strengths and weaknesses of our approach and the implications of our results for the field of 3D printing simulations in [Section 5](#).

2. Background and Related Work

Fused Deposition Modeling (FDM) is a widely used additive manufacturing technology that has gained immense popularity in the last decade due to its low cost, ease of use, and ability to produce complex geometries [1, 2]. The process involves extruding a thermoplastic material layer by layer until the final object is formed. FDM technology has found its applications in various fields, including the production of metal [3], ceramics [4], polymers [5, 6], and composites [7, 8]. One of the notable advantages of FDM technology is the ability to create parts with varying densities, which can have significant implications for various applications [9]. Another area where FDM has found its use is in the medical industry, where it is used for manufacturing patient-specific implants and drugs [10, 11]. FDM technology has also gained popularity in the aerospace industry [8].

Despite its advantages, FDM printing faces several challenges that can affect the quality and mechanical properties of the printed parts. One of the most common issues is the surface quality, which can be affected by the stair-step effect due to the layer-by-layer deposition process [12, 13]. Another challenge is achieving the desired surface roughness, which can be influenced by factors such as the nozzle diameter, layer height, and print speed [14]. Furthermore, the mechanical properties of FDM printed parts can be compromised due to weak interlayer bonding and the high melt viscosity of some materials, such as thermoplastic elastomers [15]. Achieving high print speeds can also be challenging, resulting in reduced mechanical strength and lower part accuracy [16]. These challenges have motivated research efforts to improve FDM printing technology and optimize the process parameters for better part quality and performance.

Experimental analysis of FDM parts is essential to understand their quality, behavior, and performance in different applications. Mechanical testing, dimensional analysis, surface roughness analysis, internal defect characterization, and microstructural analysis are commonly used experimental methods [17, 18, 19, 20]. However, experimentally analyzing FDM parts poses several challenges. One of the major challenges is the interplay of various process parameters, such as temperature, layer thickness, infill percentage, and print speed. These parameters affect the quality and performance of the printed parts, making it difficult to obtain consistent and accurate results [21]. The inherent anisotropy of FDM parts is another challenge, as their properties vary in different directions, making it challenging to obtain representative test results [22]. Additionally, FDM parts may contain voids, inclusions, or other defects due to the nature of the process, which can impact their performance and hinder the accuracy of test results [23]. The size and shape of the sample can also affect the test results, making it challenging to compare different samples or generalize findings to other parts or applications.

Computational tools can play a crucial role in addressing the challenges faced by experimentalists in analyzing FDM parts. For example, simulation software can model the FDM process and optimize the process parameters for specific applications [24]. This can help to reduce the number of experimental trials needed and provide insights into the effects of different process parameters on the quality and performance of the printed parts. In addition, computational methods such as finite element analysis (FEA) and computational fluid dynamics (CFD) can be used to predict the mechanical behavior of FDM parts, including their strength, stiffness, and deformation.

There have been a few physics-based computational studies of the additive manufacturing process. Ben-Artzy et al. [25] showed that residual stresses in additive manufacturing parts result from thermal expansion during heating, contraction during cooling, and volume change due to the phase transformations. The presence of these stresses can be catastrophic. Bayat et al. [26] shows the difficulty in performing full-body FEM simulations of the additive manufacturing process, which incorporates relevant physical phenomena such as fluid flow, temperature, and stress evolution due to very high computational requirements and the inability of the models to scale up [27, 28, 29, 30, 31]. Chen and Yan [32] and Bailey et al. [33] have shown a coupled simulation of CFD and solid mechanical model but

could only simulate two tracks due to high computational requirements. The lack of computational tools makes the analysis of the effect of these parameters on the final part very difficult. Our work helps overcome many computational challenges because of the easy conversion of GCode into the voxel representation, efficient mesh creation approach, and scalable FEM framework.

Voříšek and Patzák [34] presents a GCode processor for advanced additive manufacturing simulations. The paper focuses on the creation of voxel geometry from GCode, which can be used for Finite Element Method (FEM) simulations. However, their simulation is limited to the voxel geometry creation, and they do not perform any FEM simulation, which, in our understanding, is a lot more complex and computationally expensive. Additionally, the resolution of their high-resolution geometry is comparable to ours. Baiges et al. [35] presents an adaptive Finite Element strategy for the numerical simulation of additive manufacturing processes. The paper uses an adaptive octree mesh that is fine only in regions of high change and coarse elsewhere. The paper shows FEM-based steady-state mechanical analysis performed only on simple geometries like cuboids. The number of time steps they simulate is limited to only 100, and the total time taken is around 500 minutes. In comparison, our work performs FEM simulations over the entire printing process, using a more efficient octree representation. Our FEM framework can handle more complex geometries, as we have demonstrated with examples like the Stanford Bunny and Moai. Being a fast, accurate, and scalable FEM framework, we demonstrate the potential of our framework by simulating the complete printing of the Stanford Bunny and Moai, as well as the future potential of performing coupled thermo-mechanical simulations. Our total time steps solved for is much higher than the other two papers, with total mesh nodes ranging up to 350K to 500K. Additionally, our print geometry update resolution is at the voxel level, and we are able to simulate the full body of complicated geometries, not just the final mesh.

Several other authors have tackled the FDM heat-transfer problem with simplified physics but different numerical settings. Ramos et al. [36] calibrated convection coefficients for ABS and then used an ANSYS element-activation strategy combined with element homogenisation to accelerate cooling-stage analysis. Cattenone et al. [37] developed a thermo-mechanical FE framework in ABAQUS and demonstrated residual-stress prediction for simple ABS beams, while Xu et al. [38] coupled in-situ thermocouple data with a porosity-corrected thermal model to study PLA thin walls. All three studies start from pre-meshed CAD geometry and therefore still require manual mesh preparation and path scripting, in contrast to the G-code-driven, voxel-to-octree pipeline proposed here.

A closely related effort is the heat-transfer study of Ramos et al. [39], who accelerate FFF simulations inside a commercial ANSYS environment by periodically remeshing and coarsening regions that have cooled. Their workflow, however, starts from a pre-meshed solid and a hand-scripted element-activation sequence; the paper does not discuss how the nozzle path is extracted from slicer output, nor does it maintain separate air and polymer elements once a region is homogenised. In contrast, the present work ingests raw G-code, converts it to a voxel representation, builds a layer-synchronous adaptive octree *without user parameters*, and keeps air and polymer voxels disjoint throughout the build. These choices allow spatially varying convection coefficients, preserve interface fidelity, and enable real-time simulation of highly complex, sparse-infill geometries directly from the printer’s input file.

3. Additive Manufacturing Simulation Framework

In this section, we present a voxel-based 3D printing simulation framework that addresses the challenges associated with fast simulations of the FDM process. This simulation framework consists of a hierarchical and adaptive representation of the printing geometry and a physics-based simulation of the printing process. Our method leverages the power of hierarchical octree data structures and adaptive mesh refinement and coarsening strategy to efficiently generate a dynamic analysis-suitable geometry representation that changes with each new voxel print. The framework is designed to be scalable and can be used to simulate the printing process for complex geometries at high voxel resolutions. The framework can also be used to simulate the printing process in real-time, i.e., faster than the physical printing process, to enable control and fast design exploration. Figure 1 shows the flow chart of the proposed simulation method. The framework consists of three main stages: (1) converting the GCode into an intermediate voxel representation, (2) converting the voxel representation into an analysis-suitable geometry representation, and (3) performing physics-based simulations of the printing process. The following sections describe each of these stages in detail.

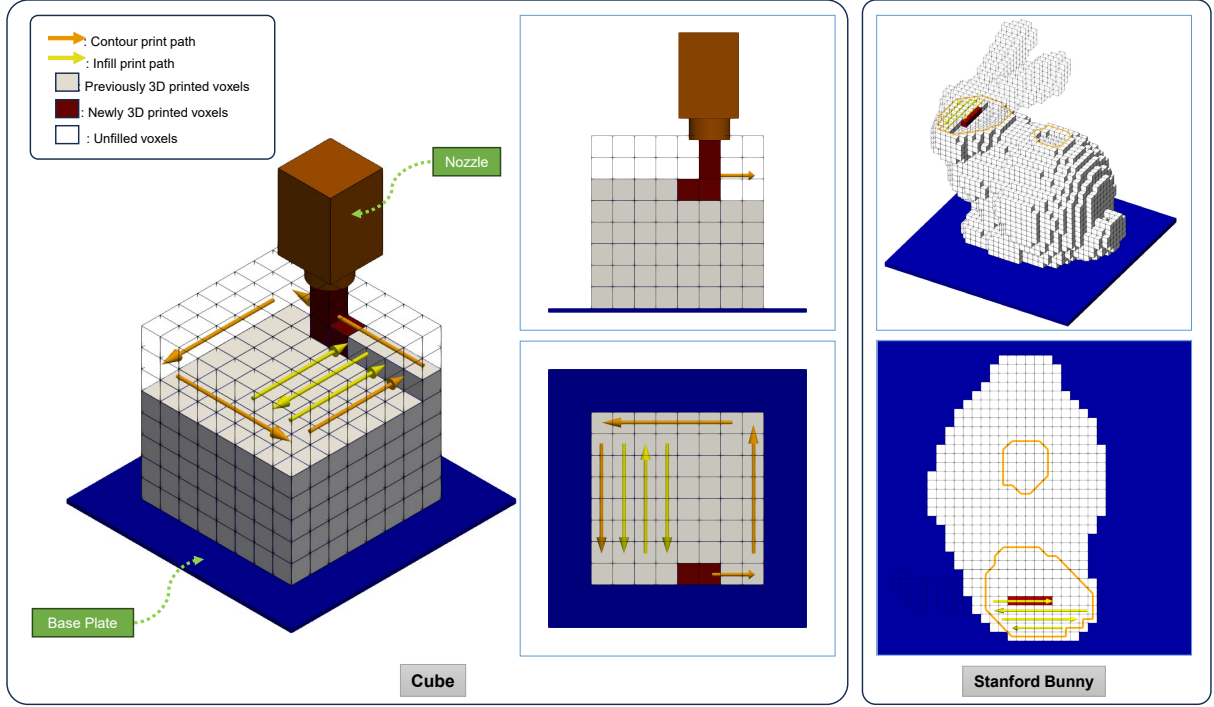


Figure 2: Voxel-by-voxel printing order for the cube and Stanford bunny geometry. The figure shows the 3D printing of the voxel geometry. The red voxels are the ones that have been printed recently, gray voxels are the ones that have been printed previously, and the white voxels are the ones that are yet to be printed. Orange arrow shows the contour print direction and the yellow arrow shows the infill print direction.

3.1. Voxel-by-Voxel (VbV) Printing Order

The first step in our simulation method involves creating a voxel-by-voxel (VbV) printing order from the GCode. A VbV printing order is a list of voxels in the order in which they are printed. The VbV printing order is a voxelized representation of the GCode and is created by projecting the toolpath onto a uniform Cartesian grid, which we call the voxel grid (V_G). We start with the GCode file and project the toolpath onto a uniform Cartesian grid. The toolpath information is extracted from the GCode and is converted into a series of line segments corresponding to the extruder's movement during printing. The voxels that are intersected by these line segments are then marked as active. This provides us with a uni-level voxel grid representation of the geometry. The grid resolution is dictated by voxel size, representing the smallest unit of the grid. We then use the method proposed by Ghadai et al. [40] to generate the layer-by-layer contours and infill patterns. These patterns are then converted into a VbV printing order. The VbV order serves as input for our subsequent geometry generation and physics-based simulation modules, enabling us to predict the temperature distribution during the printing process. Figure 2 shows the 3D printing of the voxel geometry according to the VbV printing order for the cube and Stanford bunny geometry.

3.2. Analysis Suitable Adaptive Octree Mesh

Adaptive octree mesh has been widely used in computational sciences because of its simplicity and ability to scale to a large number of processors [41, 42, 43, 44, 45]. Specifically, we used 2:1 balanced axis aligned linearized octree. An octree is said to be 2:1 balanced if two neighboring octants do not differ by more than 1 level (i.e., neighboring octants can only differ in size by a factor of 1/2). An axis-aligned octree means that each element of the octree has its axis parallel to the Cartesian coordinate axis; in other words, the elements are not deformed. A linearized octree means that each element of the mesh can be represented by the leaf of an octree, which can be linearized into an array. The linear array is obtained by traversing the octree traversal in Morton or Hilbert order. Such a traversal allows for a good locality for the computations[46]. These features make octree suitable for performing the analysis relevant to the current work.

3.2.1. Voxel and Octree Grids

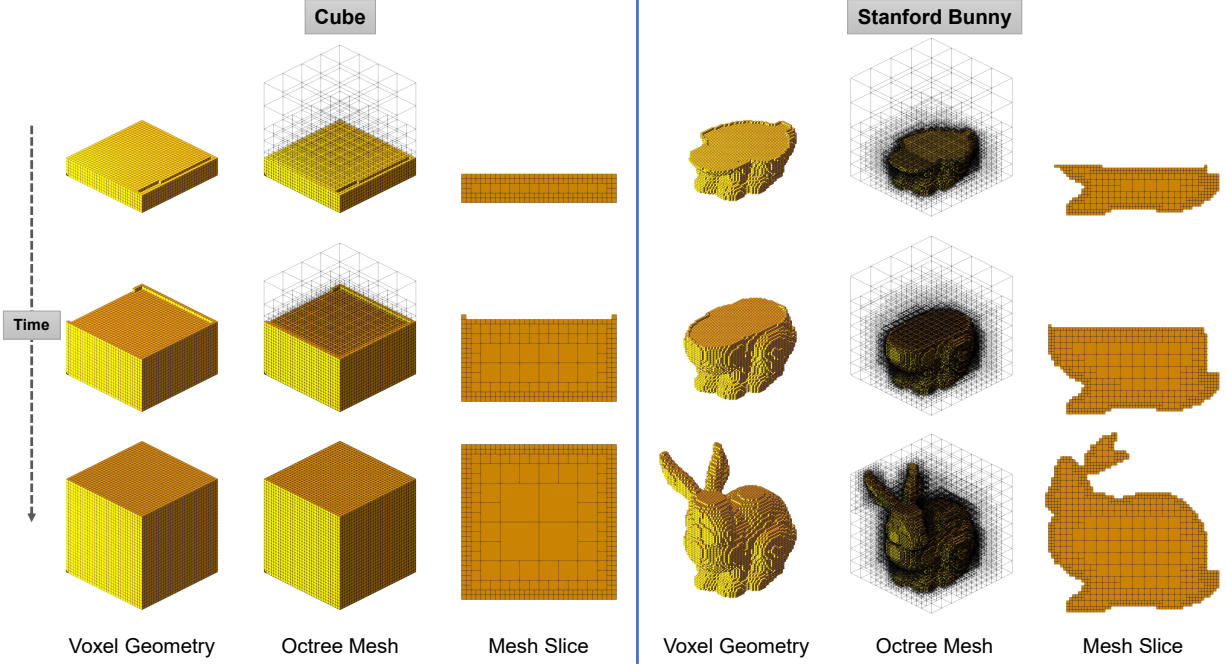


Figure 3: Voxel-based geometry, octree mesh, and 2D slices at three stages of the build for both a cube (left) and the Stanford Bunny (right). From top to bottom, each row represents an increasingly complete print. The left column in each block shows the voxel geometry at the given time, the center column shows the corresponding octree mesh (with inactive elements in wireframe), and the right column presents a mesh slice for clarity. This progression illustrates how the geometric representation, meshing strategy, and cross-sectional patterns evolve as additional layers are deposited.

In our simulation method, we utilize two distinct grid types: the voxel grid (V_G) and the octree grid (O_G) as shown in Figure 3. The voxel grid, V_G , is a uniform Cartesian grid central to the VbV printing process. We adopt a non-dimensional framework where each voxel’s dimension, Δx_i , corresponds to one non-dimensional unit. A voxel $v \in V_G$ is deemed ‘active’ once printed and participates in all subsequent simulation steps.

The finite element method (FEM) simulations, however, are conducted on the octree grid, O_G . This grid complements the voxel grid’s VbV process but introduces variable-sized elements (or octants), allowing for computational adaptability. Specifically, octants near newly active voxels are finely refined, while those in less critical areas are coarser, thereby optimizing computational resources. In all simulations, the octant corresponding to a newly activated voxel is refined to ensure that $\Delta x_{O_G} \leq \Delta x_{V_G}$.

To effectively track the evolving structure during printing, we employ a bitset vector V_B within the voxel grid V_G . This vector, sized at N_{V_G} (the total voxel count in V_G), uses 7 bits per voxel. The first bit signifies the voxel’s active status, while the remaining six represent the state of each of its six faces, indicating boundary presence. As printing progresses, this bitset is dynamically updated. Activating a voxel sets its first bit to 1 and triggers a check on its six neighboring voxels. If a neighbor is inactive, the corresponding voxel face is marked as a boundary (bit set to 1); if active, the shared face is no longer a boundary (bit set to 0). These updates are critical for constructing the octree grid O_G , ensuring a detailed and responsive representation of the printed structure.

3.2.2. Octree Construction Using Refinement and Coarsening

The construction of our octree grid is a pivotal process in our simulation, essential for dynamically adjusting the grid resolution according to the needs of the simulation. This construction starts at the highest level with a root cube and progresses in a top-down manner. Specifically, when a voxel v is activated at a new height h in the voxel grid V_G , the octree grid elements on the x-y plane at this height undergo refinement. By refining the entire x-y plane at the new height, we ensure that all elements at this level are uniformly refined to accommodate the new voxel. Using

Algorithm 1 OCTREEREFINE: Octree Refinement procedure

Require: V_G , v (activated voxel), O_G , O_L (Level of octree for required voxel)

Ensure: Refined octree

```
1: id_3d :int ← compute_3d_id(v, V_G)                                ▶ Compute the voxel id in 3D coordinate for voxel v.
2: R_flags ← [No CHANGE]                                             ▶ Vector for refine flags filled with No CHANGE
3: for e ∈ O_G do
4:   id_min :int ← compute_3d_id(e_min, V_G)                        ▶ Compute the voxel id in 3D coordinate for voxel e_min.
5:   id_max :int ← compute_3d_id(e_max, V_G)                        ▶ Compute the voxel id in 3D coordinate for voxel e_max.
6:   if id_min[2] ≤ id_3d[2] ≤ id_max[2] then                       ▶ Checking if octree element height intersects with the voxel
7:     if level(e) ≤ O_L then                                       ▶ Checking the octree RefineFlags
8:       R_flags[e] ← REFINE
9:     end if
10:  end if
11: end for
12: if all_of[R] == No CHANGE then                                   ▶ No change required for octree
13:   return O_G
14: else
15:   O_G ← construct(R_flags)                                       ▶ Construct octree with refine flags and transfer solution
16:   return OCTREEREFINE(V_G, v, O_G, O_L)                         ▶ Recursively refine till all the elements are at required level
17: end if
```

this approach, we perform refinement of O_G only once for each new height level in V_G . This strategy is particularly efficient as it avoids the need to refine the entire octree grid at every voxel activation, which would be computationally expensive and unnecessary.

The refinement decision for each element is determined by its spatial relationship with the newly activated voxel. We calculate the equivalent integer coordinates in V_G for the nearest and farthest nodes of an octant, checking whether the height range of the octant intersects with that of the activated voxel. Elements are then flagged as either REFINE or No CHANGE based on this assessment. Elements flagged for REFINE undergo an increase in resolution, dividing into eight smaller octants, whereas those flagged as No CHANGE maintain their current level. This process of refinement is recursively repeated, following the flagging procedure, until all elements achieve their required levels, indicated when all flags are No CHANGE. The algorithmic steps for this octree construction process, which balances computational efficiency with the need for precision in the simulation, are detailed in [Algorithm 1](#).

In our octree grid, coarsening is an essential process to optimize computational efficiency. This process involves the recursive merging of child octants within a parent octant, provided they are at the same level and share identical material properties (i.e., either all active or inactive). For an octant to be eligible for merging, it must satisfy the following conditions:

1. The octant is not a boundary octant, ensuring that any boundary conditions are not violated.
2. Its refinement level is above the base level, indicating it has undergone prior refinement.
3. It does not reside at the current printing height, ensuring the highest refinement in the active printing layer.

An octant that meets these criteria is flagged for coarsening (COARSEN), while others are marked as No CHANGE. This coarsening process continues recursively until all octants are flagged as No CHANGE, ensuring that the grid is optimally simplified without compromising the simulation's accuracy or resolution. The detailed algorithmic steps of this coarsening process are outlined in [Algorithm 2](#).

In the current implementation, we allow the octree to be refined or coarsened by a single level per iteration. One could alternately use multi-level refinement [47], where each octant is refined directly to a required level. We are currently exploring the computational trade-off (solve time vs. refinement cost) of this multi-level refinement strategy.

Algorithm 2 OCTREECOARSEN: Octree Coarsening procedure

Require: V_G, V_B, v (activated voxel), O_G, O_{BLvl} (Base Level of octree)**Ensure:** Coarsened octree

```
1: id_3d :int ← compute_3d_id(v, V_G)                                ▶ Compute the voxel id in 3D coordinate for voxel v.
2: R_flags ← [No CHANGE]                                             ▶ Vector for coarsen flags filled with No CHANGE
3: for e ∈ O_G do
4:   id_min :int ← compute_3d_id(e_min, V_G)                        ▶ Compute the voxel id in 3D coordinate for voxel e_min.
5:   id_max :int ← compute_3d_id(e_max, V_G)                        ▶ Compute the voxel id in 3D coordinate for voxel e_max.
6:   not_bdry :bool ← is_not_bdry(V_B[id_min])                      ▶ Check if the voxel is not a boundary voxel
7:   refined :bool ← level(e) > O_{BLvl}                             ▶ Check if the octree element is already refined
8:   not_current :bool ← is_not_currentHeight(e)                    ▶ Check if the octree element is not located at current printing height
9:   if not_bdry and refined and not_current then                    ▶ Checking if octree element meets the coarsening criteria
10:    R_flags[e] ← COARSEN
11:   end if
12: end for
13: if all_of[R] == No CHANGE then                                    ▶ No change required for octree
14:   return O_G
15: else
16:   O_G ← construct(R_flags)                                         ▶ Construct octree with coarsen flags and transfer solution
17:   return OCTREECOARSEN(V_G, V_B, v, O_G, O_{BLvl})                ▶ Recursively coarsen till all the elements are at required level
18: end if
```

3.2.3. Element Classification

After constructing the octree grid O_G , we categorize each element in the mesh into two main types: **ACTIVE** and **INACTIVE**. Elements classified as **ACTIVE** overlap with the printed voxel region at a given time t , representing the physical part of the object being printed. Conversely, **INACTIVE** elements represent the unprinted volume, essentially the surrounding air. Further, we sub-categorize **ACTIVE** elements into **IN** and **BOUNDARY** elements. **BOUNDARY** elements have at least one face on the object's outermost layer, where we apply the Robin boundary condition to model heat transfer between the object and the air. On the other hand, **IN** elements are internal and not on this boundary.

We denote the domain of **ACTIVE** elements as Ω_A . Therefore, Ω_I , representing the **INACTIVE** domain, is defined as $\Omega_O - \Omega_A$, where Ω_O is the entire cubic space defined by the root-level octree. The classification into **ACTIVE** and **INACTIVE**, as well as into **IN** and **BOUNDARY**, dynamically changes over time with the addition of new voxels v to the system, altering Ω_A and Ω_I correspondingly.

It is important to note that only **ACTIVE** regions contribute to the solution during the simulation. **INACTIVE** regions are excluded, typically by applying a Dirichlet boundary condition, effectively removing these areas from consideration during the solve step. This approach is similar to immersed-boundary methods as discussed in [48]. While dynamic matrix contraction/expansion could be used for adding or removing degrees of freedom, this is not preferred due to the significant memory overhead associated with dynamically managing contiguous memory.

3.3. Thermal Simulations

In this study, we focus on the critical aspect of temperature distribution (T) in material extrusion-based additive manufacturing processes. Our primary attention is on Fused Filament Fabrication (FFF). These techniques, pivotal in modern manufacturing, involve precise thermal control to ensure product quality. The governing equation for temperature distribution is:

$$\begin{aligned} \rho C_p \frac{\partial T}{\partial t} &= \nabla \cdot \kappa \nabla T + S(\mathbf{x}, t) \text{ in } \Omega_A \\ T(z=0) &= T_0 \text{ for } \Omega_A \times [0, t] \\ \kappa \nabla T \cdot \hat{n} + h(T - T_\infty) &= 0 \text{ in } \Gamma_A \end{aligned} \tag{1}$$

Here, κ represents the thermal conductivity of the material, ρ its density, and C_p the specific heat capacity. The term $S(\mathbf{x}, t)$ represents the heat added when a new voxel is deposited. A convenient analytical expression is

$$S(\mathbf{x}, t) = \rho C_p [T_v - T_\infty] \delta(t - t_A(\mathbf{x})),$$

where $t_A(\mathbf{x})$ is the activation time of voxel \mathbf{x} , T_∞ is the ambient temperature of surrounding air, and T_v is the nozzle temperature. In the time-discrete FEM code the Dirac pulse is implemented by resetting the Gauss-point temperature of the new voxel to T_v at the first step after activation, injecting the sensible heat $\rho C_p (T_v - T_\infty)$ in one time step. Because T_v is read directly from the printer's G-code, no empirical calibration of S is required when switching between machines. The boundary of the active printing area is denoted by Γ_A , which is dynamic as the printing progresses. The simulation assumes a constant temperature, T_0 , at the base (denoted as $z = 0$), which constitutes a Dirichlet boundary condition.

Remark on curing or crystallisation heat. Eq. (1) does not include a separate source term for latent heat released by curing or crystallisation. This simplification is appropriate for the two materials analysed:

- **ABS:** fully amorphous, so no exothermic phase change occurs after deposition.
- **PEKK:** semi-crystalline, but differential scanning calorimetry (DSC) shows *no crystallisation peak* when the material is cooled at rates of $20^\circ\text{C min}^{-1}$ or faster, which are typical of fused-filament-fabrication cooling [49, Fig. 2]. Under these conditions the polymer remains essentially amorphous during printing, so an additional latent term is unnecessary.

If future work involves a polymer that does crystallise or cure on the timescale of printing, an extra source S_{lat} can be added to the right-hand side of Eq. (1).

Non-dimensionalization. The non-dimensionalized form of the transient heat equation can be obtained by introducing dimensionless variables and scaling factors to the original equation. We assume that the characteristic length of the system is L , the characteristic time is t_c , and the characteristic temperature difference is ΔT_c . Then, the dimensionless variables are defined as follows. The dimensionless temperature T' : $T' = \frac{T - T_\infty}{\Delta T_c}$, where T_∞ is the ambient temperature. The dimensionless spatial coordinate x' : $x' = \frac{x}{L}$. The dimensionless time t' : $t' = \frac{t}{t_c}$. Using these dimensionless variables, we can rewrite the transient heat equation as:

$$\frac{\partial T'}{\partial t'} = \nabla' \cdot \alpha \nabla' T' \quad (2)$$

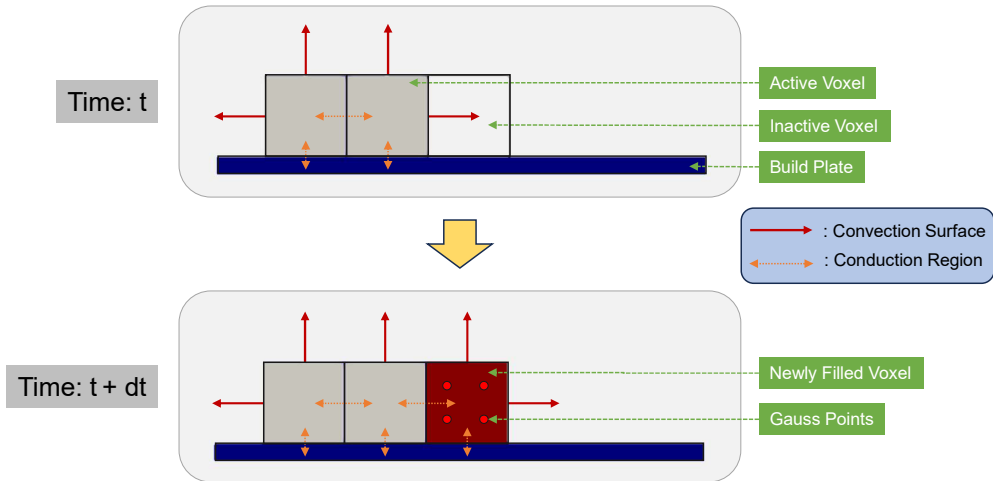


Figure 4: Illustration of the voxel-based deposition process at two consecutive time steps t and $t + \Delta t$. Existing printed voxels (gray) transfer heat through both conduction (orange arrows) and convection (red arrows). At time $t + \Delta t$, a newly filled voxel (red) is added, expanding the active region in which heat is solved. The build plate (blue) is held at a prescribed temperature boundary condition. This schematic highlights how voxel activation, heat conduction, and convection boundaries are dynamically updated throughout the printing process.

Algorithm 3 SIMULATION ALGORITHM

Require: $V[]$ (list of voxel in a given order of printing), V_G (Voxel grid), O_L (Octree level for voxel)

Ensure: $T(\vec{x})$

```
1:  $O_G \leftarrow \text{Construct}(l = l_b)$  ▷ Construct octree at base level  $l_b \leq O_L$ 
2: for  $i \in \text{len}(V)$  do ▷ Loop through the voxel
3:    $v \leftarrow V[i]$ 
4:    $V_B \leftarrow \text{UPDATE\_}V_B(V_B, v, V_G)$  ▷ Update voxel grid state
5:   if  $v \in \text{new\_layer}$  then ▷ Check if the voxel is at new layer
6:      $O_G \leftarrow \text{OCTREETREFINE}(V_G, v, O_G, O_L)$  ▷ Refine octree for  $v$  (Algorithm 1)
7:      $O_G \leftarrow \text{OCTREECOARSEN}(V_G, V_B, v, O_G, O_{BLvl})$  ▷ Coarsen octree for  $v$  (Algorithm 2)
8:   end if
9:   Reclassify  $\Omega_A$  ▷ Update ACTIVE, IN and BOUNDARY elements set
10:   $t \leftarrow 0$ 
11:  for  $t < T_n$  do ▷ Solve Equation 1 for fixed number of timestep
12:    for  $e \in \Omega_A$  do ▷ Loop through ACTIVE elements
13:      perform matrix and vector assembly ▷ Fill for both volume and surface integrals
14:    end for
15:    Apply Dirichlet Boundary condition on plate and  $\Omega_I$ 
16:    Solve system of equation for  $T$ 
17:     $t \leftarrow t + \Delta t$  ▷ Increment time
18:  end for
19: end for
    return  $T$  ▷ return the final temperature distribution
```

where $\alpha = \frac{\kappa T_c}{\rho c_p L^2}$ is the dimensionless thermal diffusivity. The non-dimensionalized equation is now independent of the specific values of the characteristic length, time, and temperature difference; it can be used to analyze heat transfer in any system with the same geometry and material properties.

Our simulation methodologically accounts for both conductive and convective heat transfer. While conduction is modelled through the material to the temperature-controlled bed, convection is represented by the Robin boundary condition applied along Γ_A . We discretise time with the **BDF2** (backward-difference, second-order) scheme and employ a *single fixed* time step Δt throughout each simulation; no adaptive time stepping is used. Figure 4 illustrates the voxel grid and adaptive octree hierarchy, highlighting the conduction region (printed material) and convection surfaces (outer boundary).

Algorithm 3 outlines the key steps for simulating the temperature distribution during the additive manufacturing process. The algorithm begins with a queue of voxels arranged in the order of printing. Initially, we create an octree at a base level, which is typically coarser than the required voxel level. The process commences with the removal of a voxel v from the start of the queue. We update V_B to reflect this new addition and to identify new boundary surfaces. If a change in the layer height of printing is observed, we reconstruct the octree O_G . This reconstruction is based on the refinement and coarsening strategies outlined in Algorithm 1 and Algorithm 2. Subsequently, the element corresponding to the voxel v is added to the domain Ω_A . With the updated octree and appropriately classified elements, we proceed to solve the heat equation up to $t = T_n$. Here, T_n represents the interval before the addition of the next voxel, which we assume to be constant for each voxel. This process is repeated iteratively for each voxel in the queue. Upon completion, when all voxels are processed, the algorithm outputs the final temperature distribution across the printed object.

4. Results

In this section, we present a comprehensive set of numerical and experimental results that showcase the capabilities and versatility of our proposed framework for real-time geometric and thermal simulations of extrusion-based additive manufacturing. We organize our findings into four key areas. First, we validate our thermal simulation against experimental data for single-filament wall prints of ABS and PEKK, demonstrating the accuracy of the model in predicting temperature evolution across different materials. Next, we apply our framework to a range of complex geometries—specifically the Stanford Bunny, 3D Benchy, and Moai head—at multiple voxel resolutions to highlight its scalability and ability to capture intricate geometric details. In the third part, we showcase our ability to model infill sparsity and the effect it has on temperature distribution, providing insight into how varying internal structures impact

heat transfer. Finally, we present photographs of physical 3D prints of these complex geometries, printed using the VbV approach at the resolution of our simulation, offering a visual and dimensional comparison between the simulated and actual printed parts. We show how our proposed approach can efficiently and accurately handle these diverse scenarios. We also highlight the computational cost and discuss possible limitations and future directions.

4.1. Comparison against Reported Experimental and Numerical Data for Single Filament Wall

To establish a literature benchmark, we compare our transient-thermal predictions against both the experimental measurements and numerical simulations reported by Lepoivre et al. [50] (experiment + simulation) and Nagaraj and Maiaru [51] (linear-element simulation). All convection coefficients ($h = 30 \text{ W/m}^2 \text{ K}$) are adopted directly from Lepoivre et al. [50], Section 2.3, without independent calibration. While this choice ensures consistency, it also means that any agreement is partly due to the same parameter selection.

Table 1 through Table 3 summarize all of the key inputs for our single-filament-wall simulations. Table 1 gives the material properties and 3D-printer settings. Table 2 shows the wall geometry and voxel discretization: each wall measures $60 \text{ mm} \times 51.2 \text{ mm}$, with a thickness of 1.25 mm (ABS) or 2.2 mm (PEKK), voxelized into a $12 \times 1 \times 63$ grid (756 total voxels). Finally, Table 3 lists the numerical parameters: a fixed time step of approximately 0.19 s (four steps per newly activated voxel), 3024 total time steps, and a final degree-of-freedom count of 1612. Each simulation required about 4 minutes on our standard workstation.

Figure 5 overlays our voxel-FEM predictions (blue) on the experimental thermocouple trace and finite-element results of Lepoivre et al. [50] (red) as well as the linear-element simulation of Nagaraj and Maiaru [51] (light-red). Both ABS and PEKK curves exhibit multiple temperature rises (“bumps”) the first of which occurs at $t \approx 9 \text{ s}$ for ABS and $t \approx 10 \text{ s}$ for PEKK. These bumps are caused by the addition of new voxels in above layers, which reheats the previously solidified material. The first bump is the largest, followed by smaller bumps. The magnitude of these bumps decreases with increasing distance from the probe layer.

For ABS (Figure 5a) our peak temperature and the subsequent cooling slope follow the experimental data within $\pm 2 \text{ K}$. Agreement with the two reference simulations is slightly looser—within $\pm 15 \text{ K}$ —but the overall cooling rate

Table 1: Material properties and 3D-printer parameters used for the single filament wall simulations.

Property	ABS	PEKK
Density (kg/m^3)	1050	1140
Thermal conductivity ($\text{W/m} \cdot \text{K}$)	0.2	0.5
Specific heat capacity ($\text{J/kg} \cdot \text{K}$)	2100	2200
Thermal diffusivity (m^2/s)	9.9×10^{-8}	1.99×10^{-7}
Convection coefficient ($\text{W/m}^2 \cdot \text{K}$)	30^a	30^a
Nozzle temperature (K)	528.15	629.15
Print bed temperature (K)	373.15	433.15
Chamber temperature (K)	368.15	412.15
Print speed (mm/s)	6.741	6.12

^a Adopted directly from Lepoivre et al. [50].

Table 2: Geometry and voxel discretization for the single filament wall.

–	ABS	PEKK
Wall dimensions (mm)	$60 \times 1.25 \times 51.2$	$60 \times 2.2 \times 51.2$
Voxel size (mm)	$5.0 \times 1.25 \times 0.8$	$5.0 \times 2.2 \times 0.8$
Voxels per wall (#)	$12 \times 1 \times 63$	$12 \times 1 \times 63$
Total number of voxels	756	756

Table 3: Key simulation parameters for the single filament wall.

–	ABS	PEKK
Time step size (s)	0.1854	0.2042
Time steps per new voxel (#)	4	4
Total number of time steps (#)	3024	3024
Final DOFs (#)	1612	1612
Wall time for each run (min)	4	4

is virtually identical, confirming that the constant-property model combined with $h = 30 \text{ W m}^{-2}\text{K}^{-1}$ reproduces the transient history measured by Lepoivre et al.

We can infer the following two insights from Figure 5b. Comparing our simulation with the experimental data of Lepoivre et al. [50], the curves for $t < 7 \text{ s}$ coincide (difference $< 3 \text{ K}$). Between 7 and 15 s the experiment is as much as 25 K higher than our prediction; Lepoivre et al. [50] report a comparable 25 °C gap in this interval and ascribe it to imperfect chamber-temperature control and pyrometer calibration [50, Sec. 3.3]. After two additional layers are deposited ($t \gtrsim 25 \text{ s}$) the difference drops below 8 K and remains small for the rest of the record. Comparing our simulation with the FE results of Lepoivre et al. [50] and Nagaraj and Maiaru [51], we find that up to $t \approx 10 \text{ s}$ all three simulations show the same cooling slope, although the Lepoivre/Nagaraj peaks are about 15 K higher than ours. From $t = 12$ to 30 s the three simulation curves cluster within a few Kelvin of each other; beyond 30 s they diverge, with our prediction staying closest to the experimental trace, whereas the two reference simulations drift below it.

Reasons for the temperature differences. All observations above fall within the discrepancy envelope documented by Lepoivre et al. [50] for PEKK: up to 25 °C in the first instants, less than 10 °C from 3 s to 50 s, and again up to 25 °C after 50 s [50, Sec. 3.3]. They identify four contributing factors, which likewise explain the gaps between our curve and theirs:

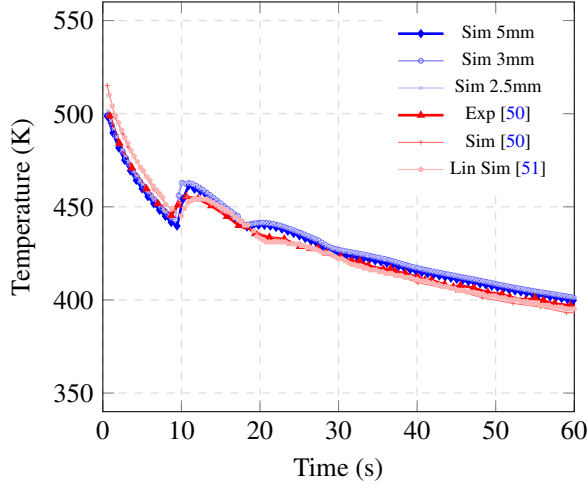
- *Heating-chamber control* – temperature drifts can generate the 25 °C error band seen after 50 s.
- *Pyrometer calibration* – inaccurate emissivity for PEKK causes systematic under- or over-reading, particularly in the first few seconds.
- *Temperature-dependent material properties and convective coefficient* – using constant k , c_p and h (as in all three simulations) leaves out known T -dependence.
- *Thermal-contact resistance* – Lepoivre et al. [50] note that its value was not measured precisely, adding further uncertainty.

Overall, the ABS history matches within experimental error, and the PEKK profile is within the $\pm 25 \text{ °C}$ band reported by Lepoivre et al., validating the ability of the proposed framework to capture short-time reheating events and long-time cooling trends with a single, literature-derived convection coefficient.

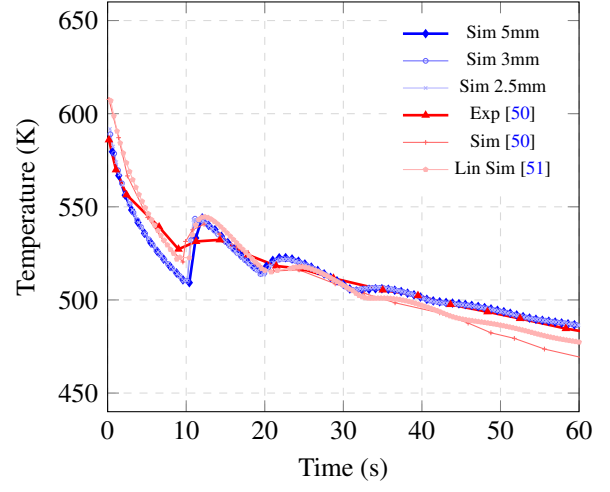
4.2. Complex Geometry Simulations

We now demonstrate the capability of our framework to handle more intricate shapes, including the well-known Stanford Bunny, 3D Benchy, and Moai head models—common benchmark geometries in computer graphics and 3D printing tests. By varying the voxel resolution, we show how our framework adapts to capture geometric fidelity and thermal effects at different scales.

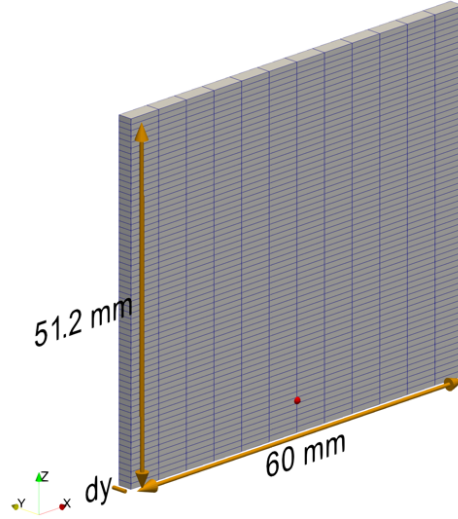
Geometry and Voxel Information. Table 4 outlines the bounding box, voxel dimension of the geometry, voxel size, and print voxel counts for these complex geometries. We consider voxel resolutions of 32^3 , 64^3 , and 128^3 for each geometry to showcase a range of fidelity levels. In each case, we position the geometry such that the z -axis corresponds to the building direction (layer stacking).



(a) ABS



(b) PEKK



(c) Wall geometry and probe location.

Figure 5: (a) Temperature vs. time for ABS: our three voxel resolutions (5 mm, 3 mm, 2.5 mm) versus the experiment and simulation curves from Lepoivre et al. [50] and Nagaraj and Maiaru [51]. (b) Temperature vs. time for PEKK under the same conditions. (c) Single filament wall geometry (60 mm \times 51.2 mm). The thickness is 1.25 mm for ABS and 2.2 mm for PEKK; the red dot marks the temperature probe location at (30 mm, 0 mm, 4.4 mm). Table 1 - Table 3 provide material, process, geometry, and numerical details.

Thermal Simulations at Multiple Resolutions. We performed thermal simulations of the Stanford Bunny, 3D Benchy, and Moai models. Figure 6, Figure 7 and Figure 8 shows the temperature evolution at 32^3 , 64^3 and 128^3 resolutions for the Bunny, 3D Benchy and Moai at three snapshots (30%, 60% and 100%) of the build. The color scale indicates the temperature in Kelvin with the minimum and maximum values set to print bed and nozzle temperatures, respectively. Each subfigure shows a 3×3 grid for geometry at different resolutions and progress levels during the build. The temperature field evolves from the nozzle temperature to the print bed temperature as the build progresses. The temperature is the highest at the newly deposited voxels and gradually decreases towards the previously printed layers. The cooling effect is due to the heat conduction from the isothermal print bed as well as due to the convection losses to

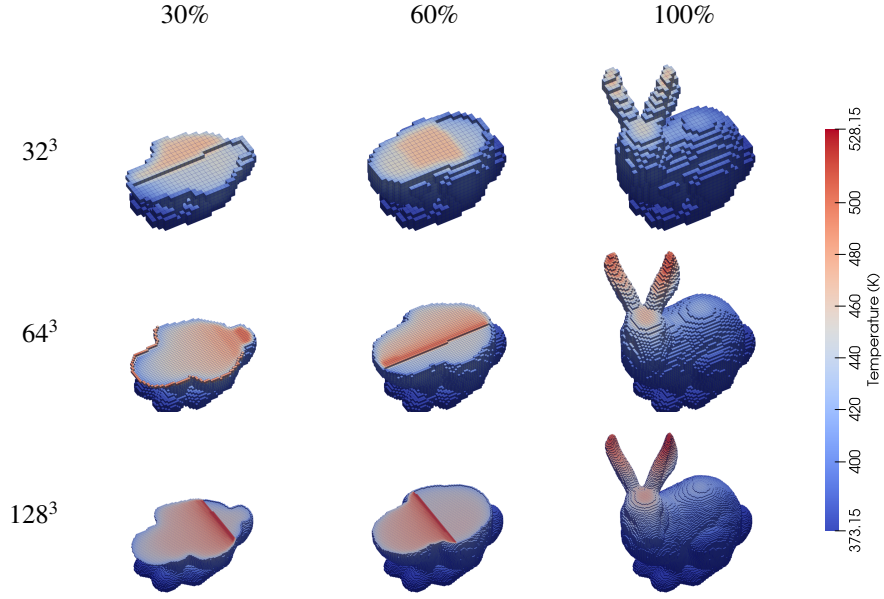


Figure 6: Stanford Bunny at three voxel resolutions (32, 64, 128) and at three build completion times (30%, 60%, 100%).

the surrounding air. The color scale is consistent across all resolutions and geometries, allowing for visual comparison of temperature profiles. The simulations are performed using the ABS material properties (Table 1).

Table 4: Geometry and voxel information for complex geometry simulations (Stanford Bunny, 3D Benchy, and Moai).

Geometry	Bounding box (mm)	Voxel dim (#, (x, y, z))	Voxel size (mm)	Print voxels (#)
Bunny	$28.2 \times 36.2 \times 35.9$	$24 \times 32 \times 32$	$1.18 \times 1.13 \times 1.12$	7,871
	$28.2 \times 36.2 \times 35.9$	$52 \times 64 \times 64$	$0.54 \times 0.57 \times 0.56$	60,008
	$28.2 \times 36.2 \times 35.9$	$100 \times 128 \times 128$	$0.28 \times 0.28 \times 0.28$	464,158
Benchy	$19.1 \times 36.5 \times 29.3$	$16 \times 32 \times 28$	$1.19 \times 1.14 \times 1.05$	4,070
	$19.1 \times 36.5 \times 29.3$	$36 \times 64 \times 52$	$0.53 \times 0.57 \times 0.56$	26,479
	$19.1 \times 36.5 \times 29.3$	$68 \times 128 \times 104$	$0.28 \times 0.29 \times 0.28$	175,481
Moai	$27.0 \times 20.3 \times 35.5$	$24 \times 20 \times 32$	$1.12 \times 1.02 \times 1.11$	3,943
	$27.0 \times 20.3 \times 35.5$	$48 \times 36 \times 64$	$0.56 \times 0.56 \times 0.55$	23,631
	$27.0 \times 20.3 \times 35.5$	$100 \times 76 \times 128$	$0.27 \times 0.27 \times 0.28$	187,197

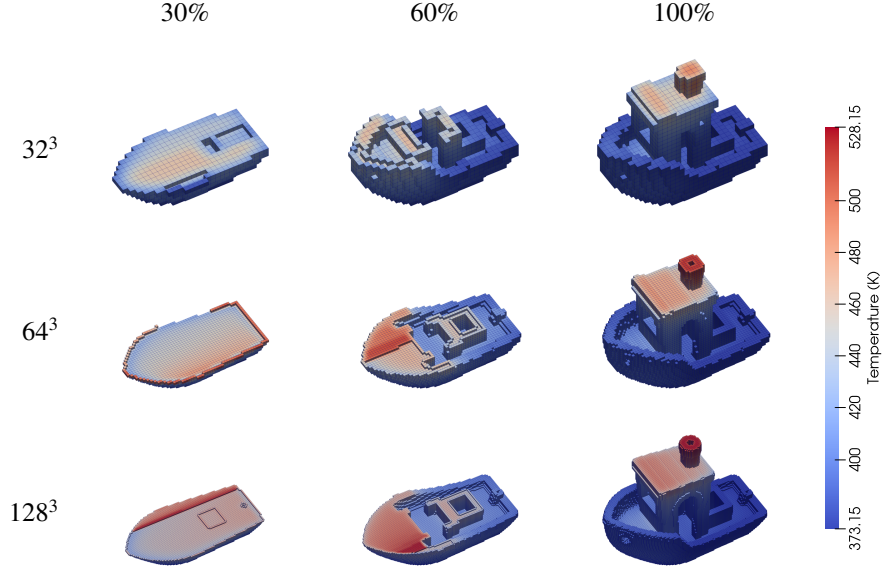


Figure 7: Benchy at three voxel resolutions (32^3 , 64^3 , 128^3) and at three build completion times (30%, 60%, 100%).

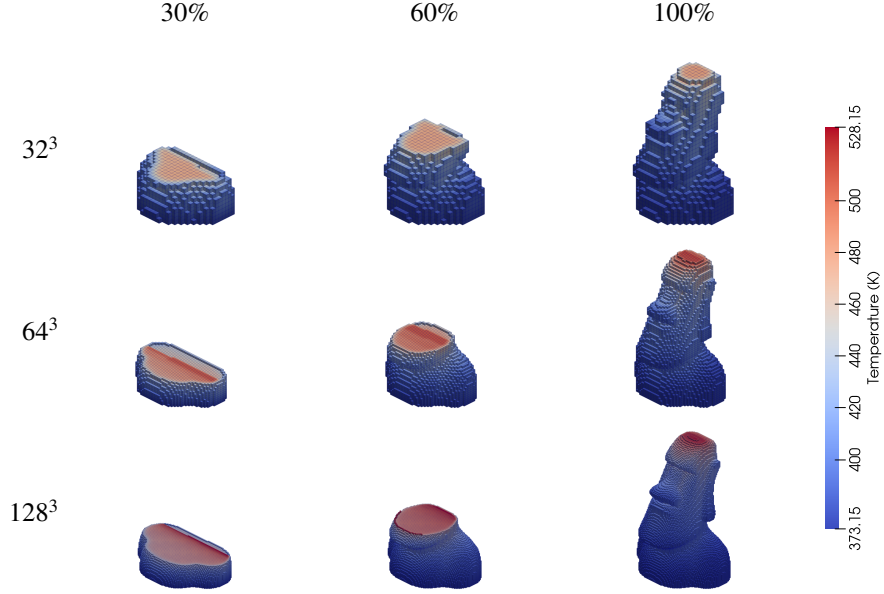


Figure 8: Moai displayed in a 3×3 grid for three resolutions (32^3 , 64^3 , 128^3) and three completion times (30%, 60%, 100%).

Simulation Parameters and Computational Cost. Table 5 illustrates the simulation metrics and scalability behavior. As the geometry resolution increases from 32^3 to 128^3 , the number of time steps and final degrees of freedom (DOFs) also increase significantly. For instance, the Bunny at 128^3 resolution requires 21,940 time steps and results in a final DOF count of 2,680,392. The wall time for simulations also scales with the resolution, with the 128^3 Bunny simulation taking approximately 2901.46 seconds on a maximum of 256 processors. This trend is consistent across all geometries, with the Moai at 128^3 taking about 2588.81 seconds and the Benchy at 128^3 taking around 3334.1 seconds.

Table 5: Representative simulation parameters and scaling behavior for the Bunny, Benchy, and Moai at various resolutions.

Geometry	Resolution	Timesteps	Final DOFs	Wall time (s)	Max Processors
Bunny	32^3	440	140,624	38.76	32
	64^3	3,280	699,000	492.62	64
	128^3	21,940	2,680,392	2901.46	256
Benchy	32^3	232	147,120	24.14	32
	64^3	2,344	619,424	432.3	64
	128^3	13,520	2,714,888	3334.1	256
Moai	32^3	328	118,504	39.12	32
	64^3	2,048	474,104	299.14	64
	128^3	23,750	2,049,104	2588.81	256

Our framework, integrated with [PETSc](#), enables efficient parallelization using BiCGS solvers with Additive Schwartz preconditioning. In previous work [\[47\]](#), we demonstrated scalability to $O(100K)$ processors. This demonstrates the computational efficiency of our framework, as it can handle complex geometries with a high degree of fidelity while maintaining reasonable simulation times.

4.3. Geometries with Sparse Infill

Infill patterns significantly affect both the mechanical and thermal response of a 3D-printed part. To investigate this, we performed simulations with varying infill densities on the Bunny models at a 128^3 resolution; the geometry details are shown in [Table 6](#). We define sparsity by “skipping” some fraction of voxels in the interior based on a user-defined pattern (e.g., skipping 3 of every 4 interior rows).

[Figure 9](#) compares three cases: no sparsity (fully dense), medium sparsity (50% layers skipped), and high sparsity (75% layers skipped). As expected, the temperature distribution differs among these configurations, with increased sparsity reducing conduction pathways and causing local thermal gradients to persist longer. This behavior can be relevant for parts where internal voids or lattice structures are desired.

Accurate heat exchange across polymer–air interfaces is achieved with two *distinct* Robin coefficients:

- h_{infill} on **internal faces** between an active voxel (polymer) and an inactive voxel (air void),
- h_{out} on the **external surface** in contact with the build-chamber air.

The coefficients come from classical free-convection theory [\[52, 53\]](#) and are summarised in [Table 7](#).

(i) **Internal polymer–air gaps (h_{infill})**. The narrowest channel width is $S = 1$ mm, while the vertical length scale of a printed layer stack is the body height $L = 40$ mm. Following the vertical–slot analysis of Elenbaas [\[54\]](#), the Rayleigh number is based on the gap width

Table 6: Sparse infill simulation details for 128^3 Stanford Bunny at different % sparse layers, starting with no sparsity (0%) and increasing to 70% sparse layers.

% Sparse Layers	Print Voxels	Time Steps	Final DOFs	Wall Time (s)	Processors
0	464,158	21,940	2,680,392	2901.46	256
30	280,842	14,200	4,470,880	2466.72	256
50	194,393	9,840	5,108,496	1688.63	256
70	169,226	8,560	5,232,648	1385.83	256

$$\text{Ra}_S = \frac{g\beta(T_s - T_\infty)S^3}{\nu\alpha} = 2.44 (< 1708), \quad (3)$$

so buoyancy is suppressed and the average Nusselt number takes its pure-conduction limit, $\text{Nu} = 1$. This implies that the internal convection coefficient is simply

$$h_{\text{infill}} = \frac{k\text{Nu}}{L} = \frac{0.036}{0.04} \text{ W m}^{-2}\text{K}^{-1} \approx 0.91 \text{ W m}^{-2}\text{K}^{-1}.$$

(ii) Outer free-convection film (h_{out}). For outer walls we adopt the Churchill–Chu correlation for a vertical isothermal plate [55], valid up to $\text{Ra}_L \leq 10^{12}$:

$$\text{Ra}_L = \frac{g\beta(T_s - T_\infty)L^3}{\nu\alpha} = 1.56 \times 10^5, \quad (4)$$

$$\text{Nu}_L = \left[0.825 + \frac{0.387 \text{Ra}_L^{1/6}}{(1 + (0.492/Pr)^{9/16})^{8/27}} \right]^2 = 10.24, \quad 10^4 \leq \text{Ra}_L \leq 10^{12}, \quad (5)$$

$$h_{\text{out}} = k\text{Nu}_L/L \approx 9.3 \text{ W m}^{-2}\text{K}^{-1}, \quad (6)$$

The solver therefore applies:

- h_{infill} on every face shared by an active and an inactive voxel (polymer–void) in the interior,
- h_{out} on outer faces,

ensuring that heat conduction through stagnant air is fully represented while matching experimentally observed external cooling rates.

The probe curves in Fig. 10 display two regimes. For the first ~ 250 s the layers deposited above the probe are *sparse*; they contain little polymer and expose a large internal surface initially to external chamber and later to the voids,

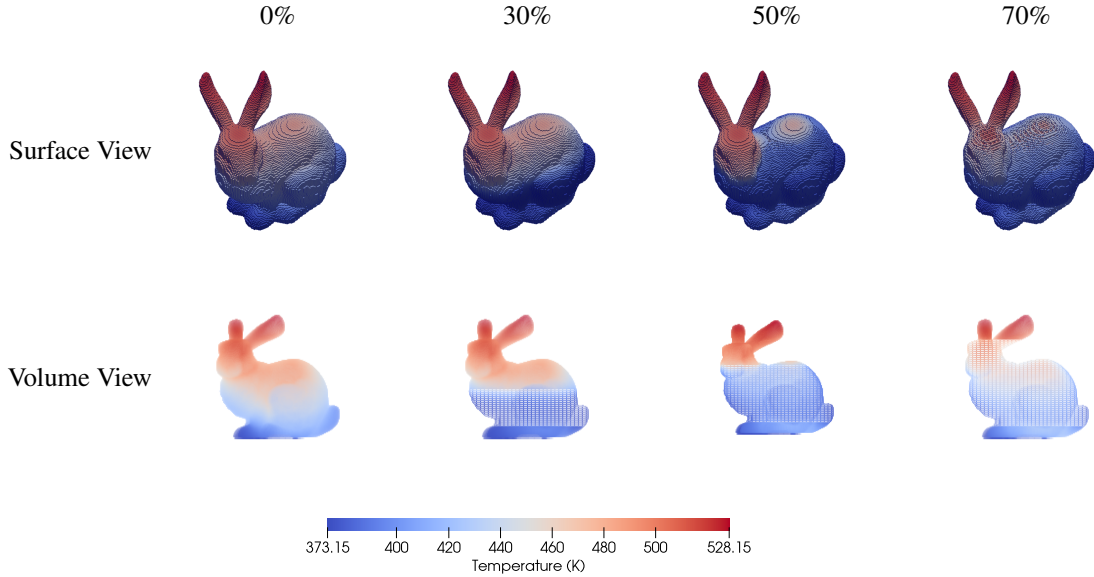


Figure 9: Surface and volumetric views of the Stanford Bunny model with different infill sparsities. The top row shows the surface temperature distribution, while the bottom row highlights the volumetric infill pattern. Increased sparsity slows overall heat diffusion and retains higher temperatures in recently deposited layers.

Table 7: Thermophysical parameters and resulting convection coefficients.

Quantity	Symbol / formula	Value
Geometry height	L (m)	0.04
Gap width	S (m)	0.001
Wall temperature	T_s (K)	528.15
Ambient temperature	T_∞ (K)	368.15
Film temperature	T_f (K)	448.15
Thermal expansion	β (K ⁻¹)	2.23×10^{-3}
Dynamic viscosity [†]	μ (Pa s)	2.48×10^{-5}
Density (ideal gas)	ρ (kg m ⁻³)	0.79
Thermal conductivity	k (W m ⁻¹ K ⁻¹)	0.036
Diffusivity	α (m ² s ⁻¹)	4.57×10^{-5}
Prandtl number	Pr	0.69
<i>Internal gap</i>		
Rayleigh number	Ra_S	2.44
Nusselt number	Nu	1 (conduction)
Convection coeff.	$h_{\text{infill}} = k/L$	0.91
<i>External wall</i>		
Rayleigh number	Ra_L	1.56×10^5
Nusselt number [‡]	Nu_L	10.24
Convection coeff.	h_{out}	9.3

[†] Kadoya et al. [56]. [‡] Churchill–Chu correlation [55].

so they cool quickly and the probe temperature drops monotonically. When the toolpath reaches the subsequent *dense* roof layers the situation reverses: the exposed surface area shrinks, convective losses are reduced, and the extra mass stores heat. Thermal energy from these hotter dense layers diffuses downward, slowing the local cooling rate for all cases or even causing a temporary reheating (30% case). Although experimental confirmation for such complex cavities is non-trivial, the inflection captured by the model is consistent with the expected thermal behaviour of alternating sparse and roof segments. A dedicated in-situ measurement campaign is planned as future work.

4.4. Physical 3D Prints of Complex Geometries

In order to demonstrate the real-world feasibility and relevance of our thermal simulation framework, we fabricated actual 3D prints of both the Stanford Bunny and the 3D Benchy at sizes matching those used in our simulations. By employing the same voxel-by-voxel deposition strategy, layer heights, and nozzle paths, we aim to show that our simulation predictions are not purely hypothetical but correspond closely to observable outcomes in physical prints. In this section, we present the printer details, geometry dimensions, and material specifications, as well as a direct comparison of printing times and simulation runtimes. Finally, we highlight qualitative observations about the printed parts and discuss how these observations align with our simulation results.

3D Printer and Material Details. All models were produced on a MakerGear M2 3D printer using ABS filament. Relevant printer specifications and typical operating parameters are summarized in Table 8. The bed and nozzle temperatures were set to 373.15K and 513.15K, respectively, to optimize adhesion and minimize warping. The nozzle diameter was set to 0.35 mm, and the layer height was set to match the voxel height used in our simulations (0.28 mm).

Geometry Details. Table 9 outlines the dimensions and voxelization information for the Stanford Bunny and 3D Benchy. Notably, the layer height on the physical printer is set equal to the voxel height used in our simulations, ensuring a consistent basis for comparing geometry size, build times, and layer-by-layer formation. These geometries

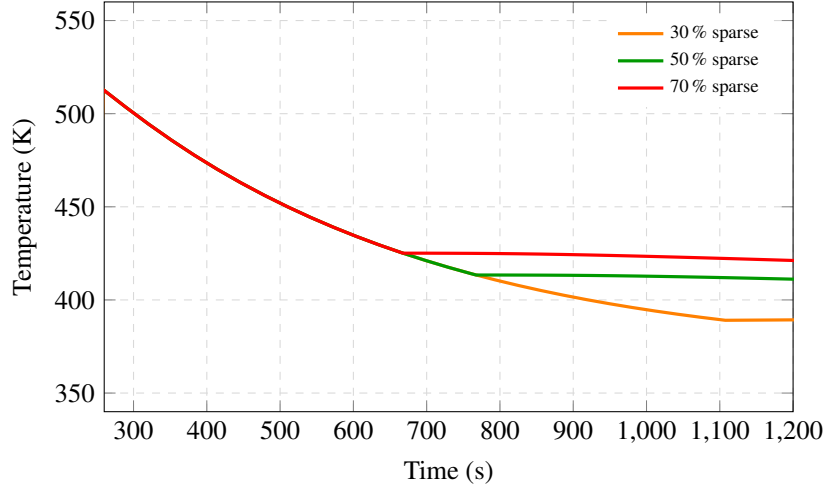


Figure 10: Temperature history at an interior probe (0.0141, 0.0182, 0.0069) m for three sparsity levels (i.e. 30%, 50%, 70% sparse layer cases). Higher sparsity earlier the temperature inflection, followed by slow cooling.

Table 8: Basic 3D printer parameters (MakerGear M2) used for fabricating the Bunny and Benchy models.

Printer Model	MakerGear M2
Filament	ABS
Nozzle Diameter	0.35 mm
Layer Height	0.28 mm
Bed Temperature	373.15K
Nozzle Temperature	513.15K

Table 9: Geometry details for the Stanford Bunny and 3D Benchy prints. “Voxels” and “Voxel Size” match the resolution used in the thermal simulations.

Model	Bounding Box	Voxels	Voxel Size
Bunny	$28.2 \times 36.2 \times 35.9$	464158	$0.28 \times 0.28 \times 0.28$
Benchy	$19.1 \times 36.5 \times 29.3$	175481	$0.28 \times 0.29 \times 0.28$

bounding boxes match those in our simulations, and the nominal voxel sizes (along all three axes) directly correspond to the physical layer height and in-plane path spacing used for printing. Because no hardware constraints prevented matching the simulation layer height, there was no discrepancy between the printed layer thickness and the voxel height in this work.

Comparison of Simulation Time with Print Time. A key goal of our work is to show that the proposed simulation can run *faster* than the actual 3D print time, even at the same resolution and approximate deposition rate. Table 10 compares the total print times versus the total simulation times for both the Bunny and Benchy prints. Notably, the Bunny simulation requires around **48 minutes** to complete, while the actual print finishes in roughly **148 minutes**. Similarly, the Benchy simulation finishes in about **55 minutes** compared to the actual print time of **96 minutes**. These results underscore our framework’s faster-than-real-time predictive capability, thereby opening avenues for in-situ monitoring or pre-print optimization.

Qualitative correspondence between prints and simulation. The photographs in Figure 11–12 serve a *qualitative* purpose: they demonstrate that a voxel-by-voxel (G-code-driven) tool path that is *identical* to the one used in the

Table 10: Comparison between simulation runtimes and actual 3D-printing durations for each geometry at matching scales.

	Simulation Time (mins)	Print Time (mins)
Bunny	48	148
Benchy	55	96

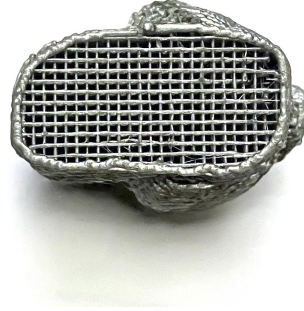


Figure 11: Top view of the bunny model printed up to an intermediate height showing the voxel pattern.

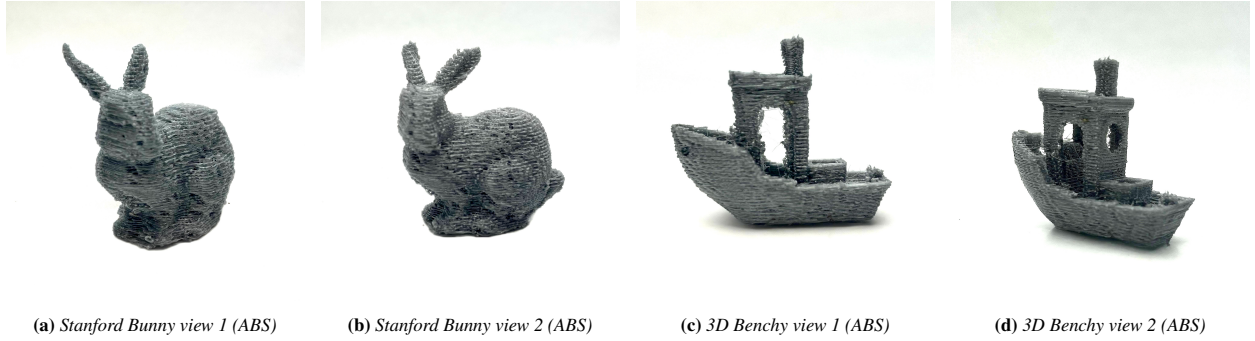


Figure 12: Photographs of actual 3D prints corresponding to our simulations. Fine surface details and minimal warping indicate that the thermal gradients are well-managed for these geometries.

thermal solver can be fabricated successfully on a commodity printer, even for complex, sparse-infill shapes. The absence of severe warping, layer delamination or large surface defects is *consistent* with the moderate thermal gradients predicted by our model for the chosen print parameters. We emphasise, however, that these images are *not* put forward as a quantitative validation of the heat-transfer solution inside the infill region. A rigorous validation would require time-resolved infrared thermography or embedded thermocouples—an experimental campaign that lies outside the scope of the present, framework-oriented study. Instead, the prints demonstrate (i) that the voxel geometry exported by our pipeline is faithfully realised in hardware and (ii) that the simulation can be executed faster than the real build, opening the door to future in-situ correction schemes. Quantitative temperature measurements in sparsely filled cavities are planned as part of our follow-up work.

5. Discussion and Conclusions

The results presented in this paper underscore both the accuracy and computational efficiency of our finite element framework for thermal simulations of extrusion-based additive manufacturing. We validated our method with single-filament experiments for ABS and PEKK (Section 4.1), demonstrating that our voxel-based approach accurately captures the transient temperature evolution with minimal runtime. The comparisons to reference experimental and

numerical data [50, 51] confirm that fundamental heat transfer phenomena—particularly conduction within and between deposited filaments, as well as convective losses to the surrounding environment—are effectively modeled at scales directly relevant to typical 3D-printing processes.

Building on these foundational results, we have extended the framework to handle more complex geometries—the Stanford Bunny, 3D Benchy, and Moai (Section 4.2). Our simulations demonstrated stable performance across multiple voxel resolutions (up to 128^3), showcasing the method’s capability to capture intricate layer-by-layer thermal behavior for geometries of practical interest in additive manufacturing. Beyond purely geometric complexity, we also investigated the influence of sparse infill patterns on temperature distribution (Section 4.3), finding that elevated local temperatures persist in regions with fewer conduction pathways. This insight can guide the design of lightweight or lattice-filled components by identifying where potential thermal-driven defects—such as local overheating or interlayer adhesion issues—are more likely to occur.

An important benefit of our approach is that it is faster than actual print time performance, as demonstrated by the simulation runtimes for the Bunny and Benchy models (Section 4.4). This capability opens up exciting possibilities for real-time process monitoring or pre-print optimization, where manufacturers can adjust parameters on-the-fly based on predicted thermal behavior. Our framework can adaptively refine or coarsen an octree-based mesh at runtime, which opens the door to high-resolution simulations over large build volumes without prohibitive computational costs. This flexibility can be crucial for industrial applications, where both geometric fidelity and throughput are paramount.

There are several research opportunities that can be explored in the future. First, the inclusion of fully coupled thermo-mechanical models would enhance predictions of warping, residual stress, and layer-to-layer bonding—phenomena critical to part reliability. Second, more complex boundary conditions (e.g., forced convection in enclosed chambers) could further improve the fidelity of predictions for industrial-grade printers and exotic materials. Third, exploring the temperature dependence of material properties, along with crystallization kinetics in high-performance polymers, may refine thermal predictions in extreme build environments. Addressing these challenges would expand the framework’s applicability and further embed it as a robust, versatile tool for process simulation.

In conclusion, our voxel-based FEM approach offers an efficient, scalable, and accurate solution for modeling heat transfer in extrusion-based additive manufacturing. The framework has been rigorously validated against established experimental and numerical benchmarks and can handle intricate geometries, varying infill strategies, and a wide range of material systems. This framework demonstrates the potential to provide predictive capabilities on timescales that are either faster than or comparable to the actual printing time. Such capabilities are significant for real-time process monitoring, adaptive control, and virtual prototyping applications—ultimately helping manufacturers optimize print quality, reduce trial-and-error cycles, and bring advanced additive manufacturing applications closer to widespread adoption.

Acknowledgements

This work was supported in part by the National Science Foundation under grant numbers LEAP-HI-2053760, CMMI-2347623, DMREF-2323716 and by the Office of the Under Secretary of Defense for Research and Engineering, Strategic Technology Protection and Exploitation, and Defense Manufacturing Science and Technology Program under agreement number W15QKN-19-3-0003. The U.S. Government is authorized to reproduce and distribute reprints for governmental purposes, notwithstanding any copyright notation thereon. The views and conclusions expressed in this work are those of the authors and do not necessarily reflect the official policies or endorsements of the U.S. Government.

References

- [1] P. Chennakesava, Y. S. Narayan, Fused deposition modeling-insights, in: Proceedings of the international conference on advances in design and manufacturing ICAD&M, volume 14, 2014, p. 1345.
- [2] T. Grimm, et al., Fused deposition modeling: a technology evaluation, *Time-compression technologies* 11 (2003) 1–6.
- [3] J. Mireles, D. Espalin, D. Roberson, B. Zinniel, F. Medina, R. Wicker, Fused deposition modeling of metals, in: 2012 International Solid Freeform Fabrication Symposium, University of Texas at Austin, 2012, pp. 1–12.
- [4] A. Bellini, L. Shor, S. I. Guceri, New developments in fused deposition modeling of ceramics, *Rapid Prototyping Journal* (2005).
- [5] O. S. Carneiro, A. Silva, R. Gomes, Fused deposition modeling with polypropylene, *Materials & Design* 83 (2015) 768–776.

- [6] P. K. Penumakala, J. Santo, A. Thomas, A critical review on the fused deposition modeling of thermoplastic polymer composites, *Composites Part B: Engineering* 201 (2020) 108336.
- [7] T. N. A. T. Rahim, A. M. Abdullah, H. Md Akil, Recent developments in fused deposition modeling-based 3d printing of polymers and their composites, *Polymer Reviews* 59 (2019) 589–624.
- [8] F. Ning, W. Cong, J. Qiu, J. Wei, S. Wang, Additive manufacturing of carbon fiber reinforced thermoplastic composites using fused deposition modeling, *Composites Part B: Engineering* 80 (2015) 369–378.
- [9] S. Dev, R. Srivastava, Effect of infill parameters on material sustainability and mechanical properties in fused deposition modelling process: A case study, *Progress in Additive Manufacturing* 6 (2021) 631–642.
- [10] D. Espalin, K. Arcaute, D. Rodriguez, F. Medina, M. Posner, R. Wicker, Fused deposition modeling of patient-specific polymethylmethacrylate implants, *Rapid Prototyping Journal* 16 (2010) 164–173.
- [11] N. Dumpa, A. Butreddy, H. Wang, N. Komanduri, S. Bandari, M. A. Repka, 3d printing in personalized drug delivery: An overview of hot-melt extrusion-based fused deposition modeling, *International journal of pharmaceutics* 600 (2021) 120501.
- [12] P. M. Pandey, N. V. Reddy, S. G. Dhande, Improvement of surface finish by staircase machining in fused deposition modeling, *Journal of materials processing technology* 132 (2003) 323–331.
- [13] C. Parulski, O. Jennotte, A. Lechanteur, B. Evrard, Challenges of fused deposition modeling 3d printing in pharmaceutical applications: Where are we now?, *Advanced drug delivery reviews* 175 (2021) 113810.
- [14] S. Vyavahare, S. Kumar, D. Panghal, Experimental study of surface roughness, dimensional accuracy and time of fabrication of parts produced by fused deposition modelling, *Rapid Prototyping Journal* (2020).
- [15] P. Awasthi, S. S. Banerjee, Fused deposition modeling of thermoplastic elastomeric materials: Challenges and opportunities, *Additive Manufacturing* 46 (2021) 102177.
- [16] P. Wang, B. Zou, H. Xiao, S. Ding, C. Huang, Effects of printing parameters of fused deposition modeling on mechanical properties, surface quality, and microstructure of peek, *Journal of Materials Processing Technology* 271 (2019) 62–74.
- [17] G. Krolczyk, P. Raos, S. Legutko, Experimental analysis of surface roughness and surface texture of machined and fused deposition modelled parts, *Tehnicki vjesnik* 21 (2014) 217–221.
- [18] L. M. Galantucci, I. Bodi, J. Kacani, F. Lavecchia, Analysis of dimensional performance for a 3d open-source printer based on fused deposition modeling technique, *Procedia Cirp* 28 (2015) 82–87.
- [19] R. Venkatraman, S. Raghuraman, et al., Experimental analysis on density, micro-hardness, surface roughness and processing time of acrylonitrile butadiene styrene (abs) through fused deposition modeling (fdm) using box behnken design (bbd), *Materials Today Communications* 27 (2021) 102353.
- [20] D. Gamdha, S. Unnikrishnakurup, K. J. Rose, M. Surekha, P. Purushothaman, B. Ghose, K. Balasubramaniam, Automated defect recognition on x-ray radiographs of solid propellant using deep learning based on convolutional neural networks, *Journal of Nondestructive Evaluation* 40 (2021) 18.
- [21] A. J. Sheoran, H. Kumar, Fused deposition modeling process parameters optimization and effect on mechanical properties and part quality: Review and reflection on present research, *Materials Today: Proceedings* 21 (2020) 1659–1672.
- [22] S.-H. Ahn, M. Montero, D. Odell, S. Roundy, P. K. Wright, Anisotropic material properties of fused deposition modeling abs, *Rapid prototyping journal* (2002).
- [23] P. Kulkarni, D. Dutta, Deposition Strategies and Resulting Part Stiffnesses in Fused Deposition Modeling, *Journal of Manufacturing Science and Engineering* 121 (1999) 93–103. URL: <https://doi.org/10.1115/1.2830582>. doi:10.1115/1.2830582.
- [24] A. Özen, D. Auhl, C. Völlmecke, J. Kiendl, B. E. Abali, Optimization of manufacturing parameters and tensile specimen geometry for fused deposition modeling (fdm) 3d-printed petg, *Materials* 14 (2021) 2556.
- [25] A. Ben-Artzy, K. Demir, J. Peterson, S. Maloy, G. X. Gu, P. Hosemann, Residual stress measurement techniques for additive manufacturing applications, *Journal of Materials Science and Engineering A* 12 (2022) 1–12.
- [26] M. Bayat, W. Dong, J. Thorborg, A. C. To, J. H. Hattel, A review of multi-scale and multi-physics simulations of metal additive manufacturing processes with focus on modeling strategies, *Additive Manufacturing* 47 (2021) 102278.
- [27] B. Khara, E. Herron, A. Balu, D. Gamdha, C.-H. Yang, K. Saurabh, A. Jignasu, Z. Jiang, S. Sarkar, C. Hegde, et al., Neural pde solvers for irregular domains, *Computer-Aided Design* 172 (2024) 103709.
- [28] H. Shah, S. Ghadai, D. Gamdha, A. Schuster, I. Thomas, N. Greiner, A. Krishnamurthy, Gpu-accelerated collision analysis of vehicles in a point cloud environment, *IEEE Computer Graphics and Applications* 42 (2022) 37–50.
- [29] M. Shadkhah, C.-H. Yang, S. Karki, B. Ganapathysubramanian, Octree-based shifted boundary method: Evaluating the impact of hanging-node removal on convergence and solver performance for linear pdes, *Advances in Computational Science and Engineering* 4 (2025) 119–141.
- [30] A. Rabeh, M. A. Khanwale, J. J. Lee, B. Ganapathysubramanian, Modeling and simulations of high-density two-phase flows using projection-based cahn-hilliard navier-stokes equations, *arXiv preprint arXiv:2406.17933* (2024).
- [31] B. Khara, R. Dyja, K. Saurabh, A. Sharma, B. Ganapathysubramanian, Solving fluid flow problems in space-time with multiscale stabilization: formulation and examples, *arXiv preprint arXiv:2402.12571* (2024).
- [32] F. Chen, W. Yan, High-fidelity modelling of thermal stress for additive manufacturing by linking thermal-fluid and mechanical models, *Materials & Design* 196 (2020) 109185.
- [33] N. S. Bailey, C. Katinas, Y. C. Shin, Laser direct deposition of aisi h13 tool steel powder with numerical modeling of solid phase transformation, hardness, and residual stresses, *Journal of Materials Processing Technology* 247 (2017) 223–233.
- [34] J. Voříšek, B. Patzák, Gpams: A g-code processor for advanced additive manufacturing simulations, *Additive Manufacturing* 65 (2023) 103279.
- [35] J. Baiges, M. Chiumenti, C. A. Moreira, M. Cervera, R. Codina, An adaptive finite element strategy for the numerical simulation of additive manufacturing processes, *Additive Manufacturing* 37 (2021) 101650.
- [36] N. Ramos, C. Mittermeier, J. Kiendl, Experimental and numerical investigations on heat transfer in fused filament fabrication 3d-printed specimens, *The International Journal of Advanced Manufacturing Technology* (2022) 1–15.
- [37] A. Cattenone, S. Morganti, G. Alaimo, F. Auricchio, Finite element analysis of additive manufacturing based on fused deposition modeling:

- Distortions prediction and comparison with experimental data, *Journal of Manufacturing Science and Engineering* 141 (2019) 011010.
- [38] D. Xu, Y. Zhang, F. Pigeonneau, Thermal analysis of the fused filament fabrication printing process: Experimental and numerical investigations, *International Journal of Material Forming* 14 (2021) 763–776.
 - [39] N. Ramos, C. Mittermeier, J. Kiendl, Efficient simulation of the heat transfer in fused filament fabrication, *Journal of Manufacturing Processes* 94 (2023) 550–563.
 - [40] S. Ghadai, A. Jignasu, A. Krishnamurthy, Direct 3d printing of multi-level voxel models, *Additive Manufacturing* 40 (2021) 101929. URL: <https://www.sciencedirect.com/science/article/pii/S2214860421000944>. doi:<https://doi.org/10.1016/j.addma.2021.101929>.
 - [41] J. Rudi, A. C. I. Malossi, T. Isaac, G. Stadler, M. Gurnis, P. W. Staar, Y. Ineichen, C. Bekas, A. Curioni, O. Ghattas, An extreme-scale implicit solver for complex pdes: highly heterogeneous flow in earth’s mantle, in: *Proceedings of the international conference for high performance computing, networking, storage and analysis*, 2015, pp. 1–12.
 - [42] H. Sundar, R. S. Sampath, G. Biros, Bottom-up construction and 2: 1 balance refinement of linear octrees in parallel, *SIAM Journal on Scientific Computing* 30 (2008) 2675–2708.
 - [43] K. Saurabh, M. Ishii, M. Fernando, B. Gao, K. Tan, M.-C. Hsu, A. Krishnamurthy, H. Sundar, B. Ganapathysubramanian, Scalable adaptive pde solvers in arbitrary domains, in: *Proceedings of the International Conference for High Performance Computing, Networking, Storage and Analysis*, 2021, pp. 1–15.
 - [44] M. Ishii, M. Fernando, K. Saurabh, B. Khara, B. Ganapathysubramanian, H. Sundar, Solving pdes in space-time: 4d tree-based adaptivity, mesh-free and matrix-free approaches, in: *Proceedings of the International Conference for High Performance Computing, Networking, Storage and Analysis*, 2019, pp. 1–61.
 - [45] C. Burstedde, L. C. Wilcox, O. Ghattas, p4est: Scalable algorithms for parallel adaptive mesh refinement on forests of octrees, *SIAM Journal on Scientific Computing* 33 (2011) 1103–1133.
 - [46] M. Bader, *Space-filling curves: an introduction with applications in scientific computing*, volume 9, Springer Science & Business Media, 2012.
 - [47] K. Saurabh, M. Ishii, M. A. Khanwale, H. Sundar, B. Ganapathysubramanian, Scalable adaptive algorithms for next-generation multiphase simulations, *arXiv preprint arXiv:2209.12130* (2022).
 - [48] K. Saurabh, B. Gao, M. Fernando, S. Xu, M. A. Khanwale, B. Khara, M.-C. Hsu, A. Krishnamurthy, H. Sundar, B. Ganapathysubramanian, Industrial scale large eddy simulations with adaptive octree meshes using immersogeometric analysis, *Computers & Mathematics with Applications* 97 (2021) 28–44.
 - [49] R. Reber III, B. Koo, D. Liu, Polyetherketoneketone (pekk), a versatile ultra-polymer for additive manufacturing, *SAMPE 2019-Charlotte, NC*, May 2019 (2019).
 - [50] A. Lepoivre, N. Boyard, A. Levy, V. Sobotka, Heat transfer and adhesion study for the fff additive manufacturing process, *Procedia manufacturing* 47 (2020) 948–955.
 - [51] M. H. Nagaraj, M. Maiaru, A novel higher-order finite element framework for the process modeling of material extrusion additive manufacturing, *Additive Manufacturing* 76 (2023) 103759.
 - [52] F. P. Incropera, D. P. DeWitt, T. L. Bergman, A. S. Lavine, *Fundamentals of Heat and Mass Transfer*, 7 ed., John Wiley & Sons, Hoboken, NJ, 2011.
 - [53] A. Bejan, *Convection Heat Transfer*, 4 ed., John Wiley & Sons, Hoboken, NJ, 2013.
 - [54] W. Elenbaas, Heat dissipation of parallel plates by free convection, *Physica* 9 (1942) 1–28. doi:[10.1016/S0031-8914\(42\)80003-2](https://doi.org/10.1016/S0031-8914(42)80003-2).
 - [55] S. W. Churchill, H. H. S. Chu, Correlating equations for laminar and turbulent free convection from a vertical plate, *International Journal of Heat and Mass Transfer* 18 (1975) 1323–1329. doi:[10.1016/0017-9310\(75\)90243-4](https://doi.org/10.1016/0017-9310(75)90243-4).
 - [56] G. Kadoya, M. Matsunaga, A. Nagashima, Viscosity and thermal conductivity of dry air in the gaseous phase, *Journal of Physical and Chemical Reference Data* 14 (1985) 947–970. doi:[10.1063/1.555744](https://doi.org/10.1063/1.555744).

Supplementary Information

Appendix A. Hardware Setup and Computing Environments

We performed simulations on two primary systems:

- **Workstation for Single-Filament Study.** For the single-filament wall simulations (ABS and PEKK) [Section 4.1](#), we used a standard workstation equipped with an **Intel(R) Core(TM) i7-4790 CPU @ 3.60GHz**. [Table A.11](#) summarizes the key hardware details.
- **Workstation for Complex Geometry and Sparse Infill.** For the larger-scale Bunny, Benchy, and Moai simulations ([Section 4.2](#), [Section 4.3](#)) we utilized more powerful 56 CPUs based HPC cluster environment, we leveraged one or more nodes of an **Intel(R) Xeon(R) Platinum 8280 CPU @ 2.70GHz** architecture. Key CPU specifications are listed in [Table A.12](#).

Hardware Parameter	Value
CPU model	Intel(R) Core(TM) i7-4790 @ 3.60GHz
Cores/Threads	4 cores, 8 threads total
L3 cache	8 MB
Max CPU frequency	4.0 GHz

Table A.11: Hardware details for the single-filament wall simulations in [Section 4.1](#).

Hardware Parameter	Value
CPU model	Intel(R) Xeon(R) Platinum 8280 @ 2.70GHz
Cores/Threads	28 cores per socket, 2 sockets, 56 CPUs total
L3 cache	39424 KB
Max CPU frequency	4.0 GHz

Table A.12: Hardware details for the complex geometry and sparse-infill simulations in [Section 4.2](#) and [Section 4.3](#).

We report the relevant CPU, cache, and memory layout for completeness, ensuring that readers can reproduce or benchmark similar setups if desired. Details on the specific number of MPI processes or threads utilized in each simulation are given in [Section 4.2](#) and [Section 4.3](#).

Appendix B. Supplementary Video

The full thermal simulation video for the 128^3 voxel resolution Stanford bunny, Benchy and Moai during the 3D printing process is attached as supplementary material. The video shows the *VbV* 3D printing process along with the temperature distribution, the variation in the infill sparsity with model height can also be seen. These visualizations show that the physics simulations can capture the complex interaction between the 3D printing parameters and the final printed object.